ACS OMEGA

Open Access

http://pubs.acs.org/journal/acsodf

Article

Unraveling the Complex Interplay of Phase Transitions in Spinel Ferrites: A Comprehensive Quantum Mechanical Vibrational Study of $ZnFe_2O_4$

Tahani Saad Almutairi*

Cite This: *ACS Omega* 2023, 8, 36999−37010

Read Online

ACCESS | Metrics & More | Article Recommendations

ABSTRACT: The rich phase transition landscape of spinel ferrites and its profound impact on their physical properties have garnered significant interest in recent years. The complex interplay of divalent and trivalent cations distributed across A- and B-sites gives rise to a captivating variety of interactions. In this study, we delve into the structural, electronic, magnetic, and vibrational properties of $ZnFe_2O_4$ as a function of the degree of inversion, employing first-principles density functional theory with global and range-separated hybrid functionals and a local basis set. The ground state of $ZnFe_2O_4$ is an open-shell system, characterized by Zn atoms occupying tetrahedral sites, Fe atoms residing in octahedral sites, and Fe atom spins exhibiting ligand parallel alignment. In the normal structure, the antiparallel arrangement is less stable than the ferro arrangement by 0.058 eV (673 K) for fully relaxed structures, decreasing to 0.034 eV (395 K) upon incorporating a zero-point vibrations contribution. For normal ferromagnetic $ZnFe_2O_4$, we calculated scattering for A_{1g}, E_g, and $3T_{2g}$ symmetry at 676.6, 367.1, and (189.7, 457.7, 602.3) cm^{-1}, respectively. Additionally, four T_{1u} vibrational frequencies predicted by group theory were obtained at 524.59, 358.48, 312.49, and 192.9 cm^{-1}, demonstrating excellent agreement with the experimental studies. We also explored the influence of spin rearrangement and inversion (X = 0.5 and 1) on Raman and infrared spectra. By analyzing the infrared spectra of isotopic substitutions, we reevaluated the assignments of the four T_{1u} modes in light of available experimental data. Notably, the sensitivity of peak positions and intensities for some Raman modes, particularly A_{1g} and $T_{2g}(2)$, to spin arrangement could provide a convenient experimental tool for detecting phase transitions induced by changes in temperature or external electric fields. This investigation shines a light on the complex interplay of phase transitions in spinel ferrites, paving the way for a deeper understanding of their properties and potential applications.

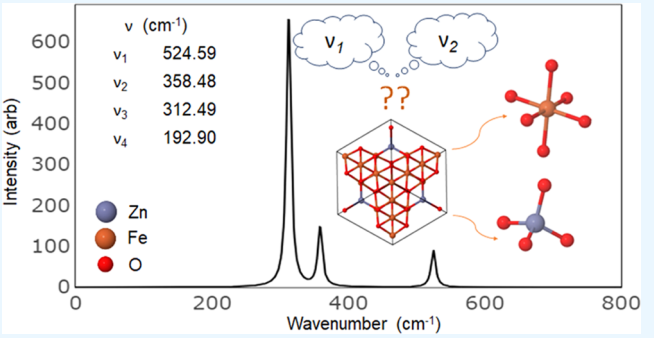

1. INTRODUCTION

Infrared (IR) and Raman spectroscopy serve as essential techniques for investigating the vibrational modes of spinel ferrites, contributing significant insights into their physical and chemical properties. Nevertheless, the task of assigning IR and Raman modes in these materials poses a significant challenge.[1−11] The complex nature of these materials, characterized by the presence of metal cations in varied sites within the crystal lattice, gives rise to multiple vibrational modes, further complicating the assignment of IR and Raman modes.[12,13] The overlap of the IR and Raman bands adds another layer of complexity, often resulting from multiple vibrational modes stemming from the tetrahedral and octahedral sites. Broad IR and Raman bands frequently observed in these materials can be attributed to site disorder, strain, or even instrumental limitations.

The spinel structure is characterized by a cubic close-packed array of oxygen anions (O^{2-}), with metal cations (M) occupying the tetrahedral (A) and octahedral (B) sites. Generally, a spinel ferrite material follows the AB_2O_4 formula, wherein A and B signify metal cations. These materials host a treasure trove of optical, electrical, and magnetic properties with insulating behavior at low temperatures and low-gap semiconductors with nonzero magnetic moments.[14−20] This multifaceted nature renders ferrites invaluable in an array of cutting-edge applications,[21,22] from photocatalysis,[23,24] and gas sensing,[25] to energy storage,[26] drug delivery,[27,28] and the ever-evolving fields of spintronics and spin caloritronics.[29,30]

Received: June 15, 2023
Accepted: September 13, 2023
Published: September 25, 2023

The absorption frequencies in spinel ferrites primarily stem from lattice vibrations of oxide ions interacting with cations, producing a spectrum of frequencies in the unit cell.[31] The frequencies are influenced by cation−oxygen bonding and cation mass. Several studies have documented the associated spinel IR frequencies for ferrite,[10,32−35] with some successfully identifying the four frequencies predicted by group theory for the spinel cubic structure[31] and others primarily focused on documenting the two high-frequency bands to confirm the spinel formation, without any density functional theory prediction linking spectral frequencies to a specific structure. The issue of IR peak splitting for spinel structures is rarely explicitly addressed in the literature.[36,37] For instance, Lopez et al. reported the splitting of the two highest-frequency bands into four bands in a ZFO sample prepared by the coprecipitation method.[38] In contrast, Zaki et al. reported a high-frequency band appearing at 700 cm^{-1}, which is outside the range reported for a normal structure..[3,31] Gawas et al. also reported a similar shoulder in the region 733−728 cm^{-1} for mixed Ni−Mn−Zn ferrites and attributed it to the stretching vibration at the tetrahedral sites.[2]

Similarly, accurate assignments of vibrational modes in spinel using Raman spectroscopy have consistently presented difficulties. Nekvapil et al. deconvoluted the Raman modes of $MnFe_2O_4$ and $Mn_{0.8}Zn_{0.2}Fe_2O_4$ into six and nine modes, respectively, compared to the five modes observed in iron oxides magnetite containing only iron cations.[6] They assigned all three peaks at the highest frequencies (674.47, 634.8, and 598.47 cm^{-1}) for $Mn_{0.8}Zn_{0.2}Fe_2O_4$ to A_{1g} symmetry. Andhare et al.[39] identified six modes related to three synthesized samples $Co_{1-x}Zn_xFe_2O_4$ (X = 0.0, 0,5 and 1.0), and assigned the additional band appears at 604.5 cm^{-1} for $ZnFe_2O_4$ to $A_{1g}(2)$ symmetry, distinguishing it from the other $A_{1g}(1)$ at 681 cm^{-1}.[11,7] The assignments presented by Yadav et al.[34] for $ZnFe_2O_4$ attributed the two bands at 605 and 653 cm^{-1} to A_{1g} symmetry, observing an increase in their intensities with the annealing temperature. Interestingly, this band around 600 cm^{-1} was not observed by Wang et al.[13] The spectra of $Ni_{0.5}Zn_{0.5}Fe_2O_4$ mixed spinel obtained by mechanochemical synthesis compared with that of $ZnFe_2O_4$ and $NiFe_2O_4$ by Lazarević et al. showed clear distortions from normal cubic spinel by exhibiting more than the expected five modes of cubic spinel.[33] They also assigned the group of the highest peaks (637, 670, 689, and 721 cm^{-1}) to A_{1g} symmetry, and from the ratio of these peaks, they estimated the inversion of cations.

In this study, we undertake a comprehensive exploration of both collinear antiferromagnetic (AFM) and ferromagnetic (FM) arrangements of normal and inverse $ZnFe_2O_4$ (ZFO), utilizing a variety of hybrid functionals rarely deployed in such systems. Zn ferrite, a spinel ferrite with exceptional magnetic properties and chemical stability, plays a pivotal role in various technological applications ranging from magnetic storage devices to catalysis.[40−42] Its unique spinel structure allows for a normal to inverse transition, a feature that can significantly impact its magnetic behavior and catalytic performance. Prior DFT studies have primarily relied on the local spin-density approximation (LSDA) and generalized gradient approximation (GGA) and GGA+U,[43−47] with no known theoretical analyses comparing the infrared features of FM and AFM ZFO at varying inversion degrees. To bridge this knowledge gap, we present calculated IR and Raman spectra, providing deep and quantitative insight into ZFO. The exploration of ZFO's vibrational modes through spectroscopic characterization opens up a fascinating realm of complex interactions and correlations, enabling a more profound understanding of the nature of spinel crystal structures. The results could potentially be used as a basis for differentiating between observed patterns in experiments that are inherent to the lattice structure and those that emerge due to imperfections, like disorder of cations. The recent advances in ab initio calculations of infrared and Raman spectra for solid materials have been instrumental in interpreting experimental results,[48] paving the way for a deeper understanding of this captivating material and its numerous applications.

2. COMPUTATIONAL DETAILS

The calculations in this study are based on density functional theory (DFT) and were obtained using the CRYSTAL17 package.[49] The calculations include atomic positions, total energy, and electronic and spin distributions on different degrees of inversion of ZFO. From the optimized structure, we obtained the IR- and Raman-active frequencies and intensities. Spin-polarized calculations were carried out to study the influence of spin ordering on the electronic and structural properties. In the ferromagnetic (FM) configuration, the magnetic moments were initially set in one direction, while in the antiferromagnetic (AFM) configuration, the magnetic moments were set to be antiparallel between two Fe atoms in the unit cell. The functionals employed in the calculations include global hybrid functional B3LYP[50] (20% of HF exchange), PBE0 (25% of HF exchange),[51] and range-separated HSE06[52] (the fraction of HF exchange varies based on the distance between electrons), which correct most of the self-interaction error of pure DFT functionals. An all-electron basis set of Gaussian-type functions was used for all atomic species involved in the study.[53−55]

The five thresholds, T_i, that controlled the truncation criteria of the Coulomb and exchange infinite series were set to 8 (T1−T4) and 16 (T5). The energy convergence thresholds for the self-consistent field (SCF) cycle were set to 10^{-8} and 10^{-10} Hartree for optimizations and vibration frequency calculations, respectively. The full optimization process, involving lattice parameters and all atomic bases in the cell, used a root-mean-square (rms) displacement of 10^{-5} Å. The shrinking factors controlling the number of independent k-points used in the sampling of the Monkhorst−Pack net,[56,57] were set to 88, corresponding to 29 points in the first Brillouin zone with ZFO. Mulliken population analysis for charge and magnetic moments was executed at the end of the SCF process for each nonequivalent atom.[49,58] The magnetic moments were specified solely for the atoms in the initial guess, α (+1) and spin β (−1), to define the open-shell configurations. The frequencies (wavenumber) ω_p were calculated from second energy derivatives with respect to atomic displacements u at the Γ point,[59,60] according to the following equations:

$$W^{\Gamma}_{ai,bj} = \frac{H^0_{ai,bj}}{\sqrt{M_a M_b}} \text{ where } H^0_{ai,bj} = \frac{\partial^2 E}{\partial u^0_{ai} \partial u^0_{bi}} \quad (1)$$

where u is the atomic displacement of atoms a and b in the system, with atomic mass M_a and M_b, respectively. The i-th and j-th are the Cartesian directions in which the atoms move (atomic coordinates). Then, at no computational cost, the shift in frequencies due to isotopic substitutions can be obtained by replacing the masses in eq 1.

https://doi.org/10.1021/acsomega.3c04268
ACS Omega 2023, 8, 36999−37010

Table 1. Thermodynamic Functions (eV/cell) Obtained at T = 298.15 K and P = 0.10132500 MPa for Different ZFO Systems[a]

	X = 0		X = 0.5		X = 1	
energy	FM	AFM	FM	AFM	FM	AFM
E_0	0.8961	0.8813	0.8839	0.8790	0.8729	0.8742
E_T	0.3914	0.3981	0.3970	0.3994	0.4026	0.4025
S (meV/(cell·K))	2.1859	2.2381	2.2202	2.2418	2.2569	2.2602
PV	0.000097	0.000097	0.000097	0.000097	0.000097	0.000096
TS	0.6517	0.6672	0.6619	0.6684	0.6729	0.6738
E_T + PV-TS	−0.2601	−0.2690	−0.2648	−0.2688	−0.2702	−0.2712
$E_R = E_L + E_0 + E_T$ + PV-TS	0.00	0.034	0.575	0.267	0.864	0.455

[a] E_L denotes the energy per lattice cell (electronic energy), E_0 represents the zero-point energy, E_T signifies the thermal contribution to the vibrational energy, and S denotes entropy. All energies are obtained at the B3LYP level. E_R indicates the relative energy compared to the ground state (FM, X = 0.0).

The integrated intensity for IR absorption I_p for each P mode is computed through a CPHF/KS method[61,62] as follows:

$$I_p = \frac{\pi N_A}{3c^2}.\ d_p.\ |\vec{z}_p|^2 \quad (2)$$

where c is the speed of light, N_A is the Avogadro's number, d_p is the degeneracy of the mode, and $\vec{z}_p$ is the mass-weighted effective mode Born charge vector.[63] The Raman intensities are evaluated analytically based on the first- and second-order coupled perturbed Hartree−Fock/Kohn−Sham (CPHF/KS) equation solutions.[64]

3. RESULTS AND DISCUSSION

3.1. Energy, Geometry, Charge and Spin Distribution, and Band Structure. Our investigation of the thermodynamic functions obtained from spin-polarized calculations (Table 1) reveals intriguing insights into the stability of various ZFO configurations. The FM ZFO (X = 0) emerges as the most stable configuration, corroborating previous findings using the PBE0 functional.[65] The electronic energy of FM ZFO (X = 0) is lower than that of AFM ZFO (X = 0) by approximately 0.058 eV, which decreases to 0.034 eV (395.5 K) when considering the free energy, inclusive of zero-point energy. Increasing the inversion degree reduces the stability of both FM and AFM-ZFO by about 0.59 and 0.29 eV for (X = 0.5) and 0.89 and 0.48 eV for (X = 1), respectively. As the inversion degree increases, the stability of both FM and AFM-ZFO diminishes by about 0.59 and 0.29 eV for (X = 0.5) and 0.897 and 0.488 eV for (X = 1), respectively. Significantly, we observe consistent relative stabilities across all functionals utilized in this study (Table 2). This consistency underscores the robustness of our results, even when the hybrid functional changes, particularly in terms of variations between the two spin states. The influence of the exact exchange percentage is evident in the energy difference between the spin states across all of the employed functionals. Previous DFT studies[65,66] highlight the importance of hybrid functionals for achieving better congruence with experimental results, compared to the GGA + U method. Our study aligns with these findings regarding relative energy and supports the experimental study proposing that ZFO is fundamentally a FM system, driven by first-neighbor exchange interactions.[67,68]

Table 2. Electronic Relative Energy (in eV) of (X = 0, 0.5, and 1) ZFO Spinel Geometry ($Zn_{1-X}Fe_X$) [$Zn_XFe_{2-X}O_4$] to the FM Normal Spinel Structure Calculated with Different Functionals

	X = 0		X = 0.5		X = 1	
functionals	FM	AFM	FM	AFM	FM	AFM
B3LYP	0.00	0.059	0.59	0.29	0.90	0.49
HSE06	0.00	0.07	0.59	0.33	0.91	0.54
PBE0	0.00	0.08	0.58	0.34	0.90	0.55

Figure 1 illustrates the optimized structure of the ZFO crystal with X = 0 in two-spin arrangements: FM (Figure 1a) and AFM (Figure 1b) configurations. These diagrams, obtained by using the B3LYP functional, highlight bond distances (in Å), net charges (in |e|), spin densities (in |e|), and bond populations (in |e|). Mulliken population analysis, calculated for charge and spin density at the end of the self-consistent-field (SCF) cycle, offers valuable insights into the nonequivalent atoms.[49,58] The local symmetry of normal FM-ZFO belongs to the cubic crystal family and the $Fd3m$ space group (centrosymmetric), comprising 48 symmetry operations. Lattice parameters obtained with three adopted functionals for normal spinel FM-ZFO [B3LYP = 8.522 Å, PBE0 = 8.448 Å, HSE06 = 8.450 Å] fall within the range of measured values: 8.441 Å,[69] 8,445, 8.451 Å,[18] 8.459 Å,[17] 8.520 Å.[70,67] The Fe−O and Zn−O bond lengths in the normal spinel are almost equal with negligible differences (0.03 Å for FM and 0.02 Å for AFM), aligning with previously measured values for (Zn−O) (Fe−O) bond lengths, [2.12, 2.01 Å],[71] [2.11, 2.12].[71] Figure 1 suggests that the distortion from the cubic structure is minimal in the AFM arrangement, as exemplified by the variations in Fe−O bonds: about 0.001 Å within AFM, and approximately 0.004 Å compared to FM. As the inversion degree increases, bond lengths and populations in both A- and B-sites reveal significant variations, emphasizing the crucial role of Fe atoms' occupation of the A-site.

In FM of X = 0.5 where Fe and Zn atoms distribute between A- and B-site, their bonds are as follows: A-site -3 × Fe−O 1.93 Å, 1× Fe−O 1.97 Å, 3 × Zn−O 1.99 Å, 1 × Zn−O 2.01 Å; B-site -3 × Fe−O 1.99 Å, 3 × Fe−O 2.04 Å, 3 × Zn−O 2.10 Å, 3 × Zn−O 2.11 Å. Similarly, in AFM of X = 0.5, the bonds are A-site -1 × Fe−O 1.95 Å, 2 × Fe−O 1.94 Å, 1 × Fe−O 1.95 Å, 1 × Zn−O 2.01 Å, 2 × Zn−O 1.98 Å, 1 × Zn−O 1.99 Å; B-site: no symmetry remaining with Fe−O as their bonds are (1.99, 2.00, 2.04, 2.04, 2.06, 2.08 Å) and Zn−O bonds are (2.091, 2.098, 2.11, 2.14 Å). The highest bond population is with the Zn−O bonds in the A-site (0.093−0.043 |e|), and the lowest values are with the Fe−O bonds (0.029−0.014 |e|), indicating a preference for the former to tetrahedral site due to the difference in ionic size (Zn^{2+} 0.74 Å, Fe^{3+} 0.64 Å).

In FM of X = 1, the A-site bonds are 2 × Fe−O 1.91 Å, 2 × Fe−O 1.95 Å, and the B-site bonds are 3 × Fe−O 2.03 Å, 3 × Fe−O 2.06 Å with a population of approximately 0.03−0.05 |e|, and 3 × Zn−O 2.14 Å, 3 × Zn−O 2.11 Å with a population of

https://doi.org/10.1021/acsomega.3c04268
ACS Omega 2023, 8, 36999−37010

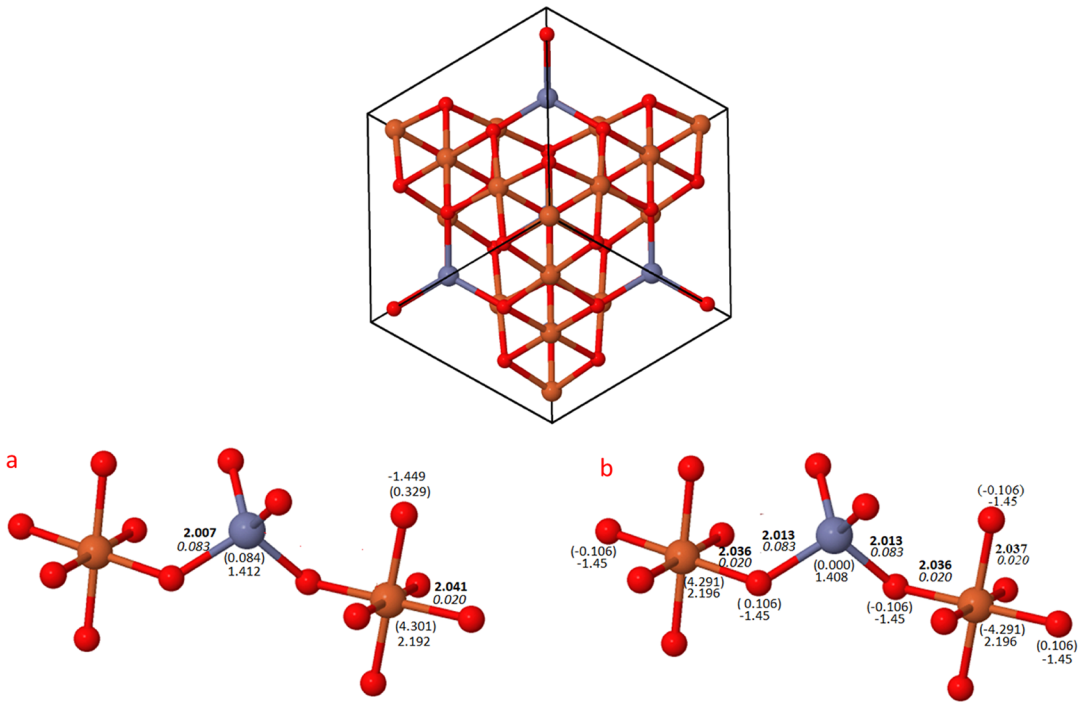

Figure 1. Schematic representation of bond lengths (Å/bold), bond populations (|e|/italic), spin moment (|e| in parentheses), and Mulliken charges (|e|) for normal spinel (a) FM and (b) AFM configurations. Data obtained using B3LYP.

Table 3. Band Gaps (eV) and Magnetic Moments (μ_B) for Various Magnetic Arrangements (FM and AFM) in ZFO Geometries ($Zn_{1-X}Fe_X$) and [$Fe_{2-X}O_4$] Calculated Using Different Functionals

functionals	ZFO		E_g^α	E_g^β	Fe (O_h) μ_B	Fe (T_d) μ_B	Zn (O_h) μ_B	Zn (T_d) μ_B
B3LYP	$X = 0$	FM	5.277	3.138	4.301			0.084
		AFM	2.948	2.948	4.291			0.000
					−4.291			
	$X = 0.5$	FM	5.354	3.086	4.312	4.291	0.034	0.083
		AFM	2.960	3.100	4.298	4.229	0.025	−0.024
					−4.275			
	$X = 1$	FM	5.481	2.864	4.349	4.259	0.056	
		AFM	3.346	3.347	4.299	4.214	0.000	
					−4.299	−4.214		
HSE06	$X = 0$	FM	5.103	3.264	4.354			0.086
		AFM	3.068	3.063	4.347			0.000
					−4.348			
	$X = 0.5$	FM	5.168	3.085	4.367	4.349	0.030	0.086
		AFM	3.085	3.165	4.355	4.291	0.025	−0.025
					−4.334			
	$X = 1$	FM	5.272	2.876	4.403	4.315	0.053	
		AFM	3.436	3.432	4.360	4.274	0.000	
					−4.361	−4.274		
PBE0	$X = 0$	FM	5.822	3.926	4.363			0.085
		AFM	3.798	3.798	4.357			0.000
					−4.357			
	$X = 0.5$	FM	5.889	3.783	4.375	4.357	0.030	0.085
		AFM	3.825	3.902	4.364	4.303	0.025	−0.024
					−4.344			
	$X = 1$	FM	5.996	3.556	4.411	4.323	0.053	
		AFM	4.159	4.160	4.371	4.285	0.000	
					−4.371	−4.285		

approximately 0.04−0.05 |e|. In AFM of $X = 1$, the A-site bonds are 2 × Fe−O 1.93 Å, 1 × Fe−O 1.92 Å, 1 × Fe−O 1.90 Å, and the B-site bonds are Fe−O bonds 1.99, 2.01, 2.03, 2.09 Å, and the Zn−O bonds 2 × 2.08 Å, 2.126 Å, 2.127 Å, 2.13 Å, and 2.14 Å, with population about 0.015−0.033 |e| in Fe−O, and 0.04−0.06 |e| in Zn−O. The nature of the Zn−O and Fe−O bonds, estimated from the very low value of bond populations and

https://doi.org/10.1021/acsomega.3c04268
ACS Omega 2023, 8, 36999−37010

charge distributions, are predominantly ionic. Oxygen atoms accumulate charge (∼−1.5 lel) from the surrounding cations.

Our analysis demonstrates that the total spin densities for Fe and Zn atoms are conserved in all calculated structures, with Fe exhibiting a magnetic moment consistent with experimental measurements of 4.2 μ_B,[17,72] and previous calculations, 4.1−4.2 μ_B[73,45] and 4.7−4.8 μ_B.[43,74] Zn atoms, in contrast, display nearly zero spin density in both configurations, confirming their diamagnetic nature (Table 3).

Figure 2 compares the complementary band structures obtained with the B3LYP approach for FM-ZFO and AFM-ZFO with varying degrees of inversion. Energy gaps along the α and β spin channels (Table 3) can be compared to values obtained with other functionals. In FM, a significant shift between the α and β bands results in distinct direct energy gaps, aligning with previously calculated value with PBE0 (3.13 eV),[65] and experimental measurement.[75] The impact of inversion on the energy gaps is minimal, with a slight increase or decrease depending on the inversion degree and spin channel.

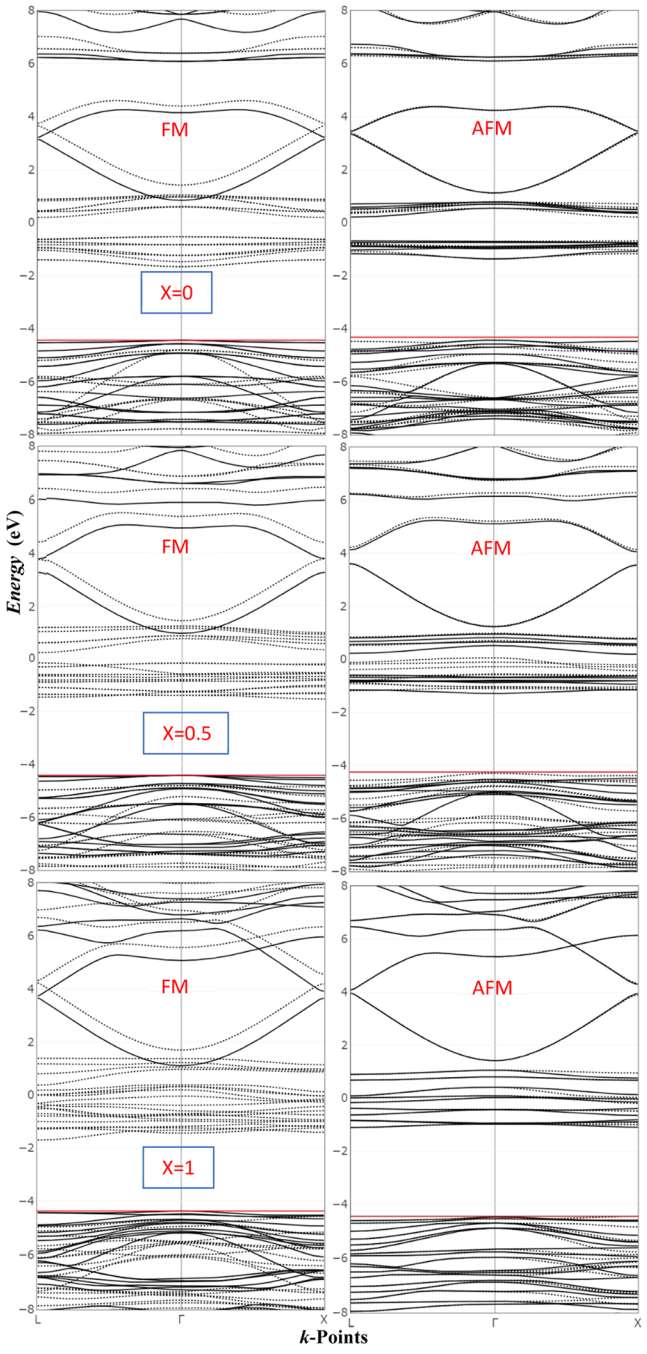

Figure 2. Band structures of ZFO in FM (left) and AFM (right) configurations calculated with B3LYP for varying degrees of inversion. The red horizontal line represents the Fermi level, while continuous and dotted black lines indicate the α and β energy bands, respectively.

3.2. Spectroscopic Characterization: Exploring Crystal Structures with Raman and Infrared Spectroscopy. The complex of crystal structures can be revealed through the Raman and infrared (IR) spectra, though experimentally assigning spectral features to particular structures can prove challenging. Preparation methods, temperature, defects, and intrinsic structural disorder may all cooperate to complicate the analysis. Thankfully, simulated spectra emerge as a powerful tool, enabling precise characterization of spectral features while sidestepping most of these interfering factors.

The IR vibrational spectra of ZFO configurations, computed at the B3LYP level and derived from equilibrium lattice structures, are displayed in Figure 3. Each panel showcases a different configuration, with the first panel representing $X = 0$, the next two featuring $X = 0.5$ and 1, and each panel including the AFM spectrum for comparison. These spectra are plotted with a full width at half-maximum of 8 cm^{-1} and a pseudo-Voigt function—a linear combination of Lorentzian and Gaussian functions. Delving into the $ZnFe_2O_4$ spinel's space group $Fd3m$ (O_h^7), we uncover 42 modes, 39 of which are optical and the remainder acoustic. Group theory analysis reveals that the infrared-active vibrational mode is the triply degenerate $4T_{1u}$, while the Raman-active modes consist of A_{1g}, E_g, and $3T_{2g}$ combinations.[1]

The FM-ZFO ($X = 0$) spectra feature four distinct modes. Analyzing the spectra, we traverse from the lowest wavenumber (193 cm^{-1}, v_4) to the highest (524 cm^{-1}, v_1), unraveling the hidden relationships between bending and stretching modes involving Zn and Fe atoms. The mode at 193 cm^{-1} v_4 has unobserved intensity and is related to the bending mode of O−Zn−O and Zn−O−Fe. The second mode at 312.5 cm^{-1} (v_3) has the highest intensity and is a combination of the bending modes of Zn−O−Fe, O−Fe−O, and O−Zn−O, as well as the stretching modes of Fe−O−Zn. The third peak that appears at 358 cm^{-1} (v_2) is exclusively related to the atoms in the octahedral sites (Fe−O−Fe mode). The last peak at 524 cm^{-1} (v_1) has the lowest intensity and is related to the bending mode of Fe−O−Zn. These four active modes exhibit triply degenerate phonons of T_{1u} symmetry, aligning with group theory and demonstrating good agreement with previously reported values for ZFO[31] (Table 4). According to Waldron[31] and Hafner,[12] the v_1 band related to the intrinsic vibrations of the AO_4, and v_2 belong to the BO_6. Turning our attention to the simulated spectra of isotopic substitutions ($^{56}Fe \rightarrow {}^{58}Fe$ and $^{65}Zn \rightarrow {}^{67}Zn$) for ZFO FM ($X = 0$) in Figure 4, we uncover intriguing correlations between the vibration modes of the two cations. As we progress from high to low wavenumbers, the IR peaks become more influenced by the heavier Zn atom and vice versa for the Fe atom. This insight helps us further understand the complexity of ZFO's vibrational modes, while also shedding light on the important work of Preudhomme and Tarte.[76−78] Based on their experimental isotopic data, they found that the contribution of the tetrahedral cation to the vibration modes is too small to be observed experimentally, and the band at the

https://doi.org/10.1021/acsomega.3c04268
ACS Omega 2023, 8, 36999−37010

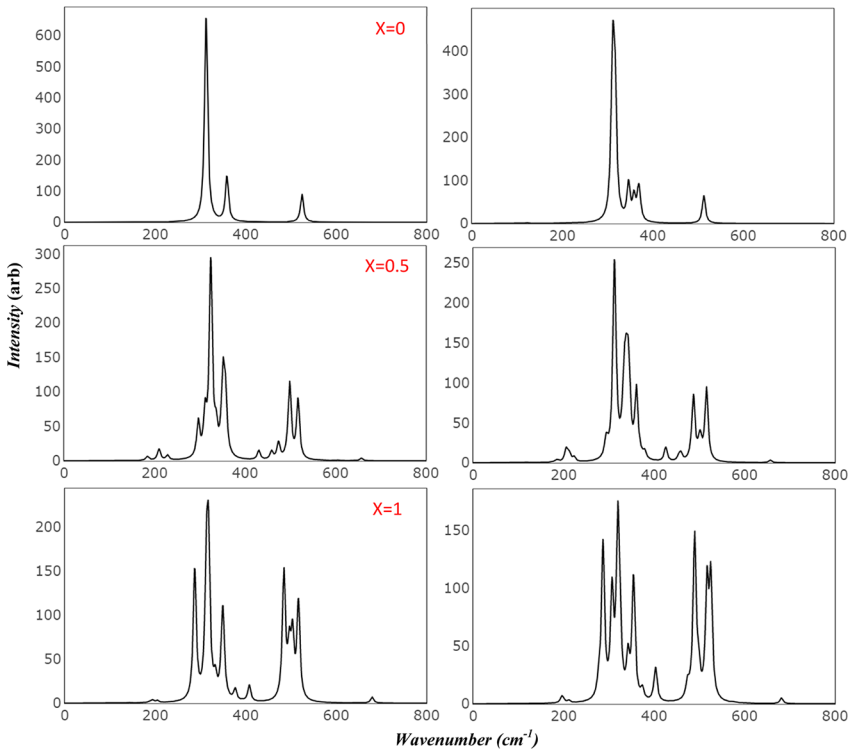

Figure 3. B3LYP simulated infrared spectra of ZFO (X = 0.0, 0.5, 1.0) with its two-order magnetic configuration; left panels refer to FM, and right panels refer to AFM.

Table 4. Comparison of the Frequencies of the IR Modes of Normal ZFO Presented Previously with Those Calculated in the Present Study

vibrational modes (cm^{-1})	ref 31	ref 32	ref 76	ref 79	ref 80	current study
v_1	555	600–548	552	590	555	524.59
v_2	393	400–450	425	400	430	358.48
v_3	325	330–350	336	240	330	312.49
v_4	169	<200	166			192.9

lower frequency (v_4) is more likely to be affected by the divalent tetrahedral cation.

In the AFM-ZFO (X = 0) spectra, we notice key differences compared to FM spectra, such as the splitting of the intermediate band at 358 cm^{-1} into four bands (346, 358, 368, and 370 cm^{-1}) and the appearance of additional low-intensity modes. The peak centered at 312.21 cm^{-1} appears as one broad peak. The highest-frequency band exhibits a red shift of about 12 cm^{-1} (513 cm^{-1}), while the lowest-frequency band shows a blue shift of 3 cm^{-1} (195 cm^{-1}). The spin reconstruction also activates additional modes with very low intensity, specifically at low frequencies 121.2, 188 cm^{-1} and others at 245, 447, and 635 cm^{-1}. Isotopic shifts in Figure 4 indicate that the new modes (121.2, 245, 447, and 635 cm^{-1}) are mainly influenced only by Fe atom, particularly the 447 and 245 cm^{-1} modes, which exhibit large shifts of 7.7 and 4.4 cm^{-1}, respectively. The mode at 188 cm^{-1} demonstrates the same correlation as that of the 194.7 cm^{-1} mode.

The simulated Raman spectrum of FM ZFO (X = 0) features five active internal modes related to T_{2g}, A_{1g}, and E_g symmetry species (Figure 5). These five peaks are well separated, with their symmetries aligning with the calculations in ref 1. The first peak occurs at 676 cm^{-1} (A_{1g}), followed by two peaks at 602 cm^{-1}

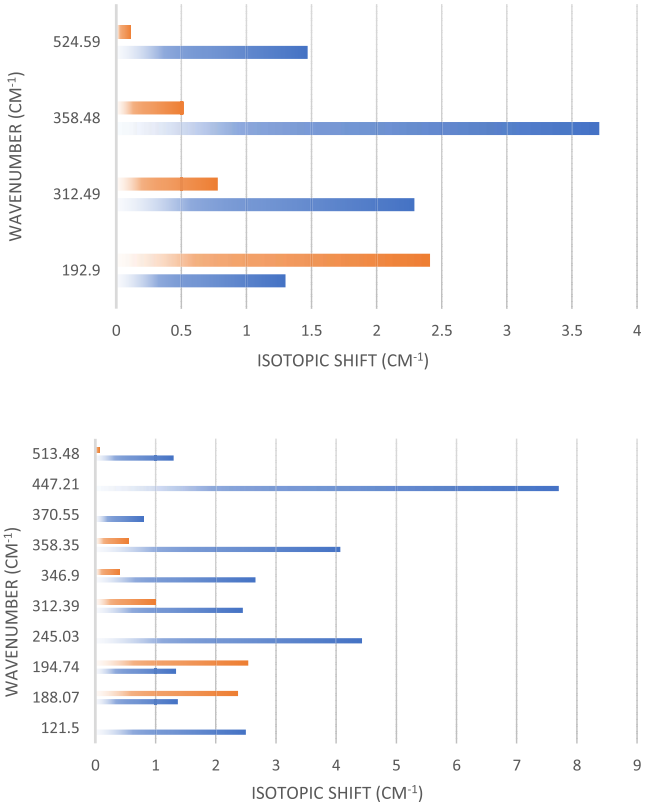

Figure 4. Simulated isotopic shifts resulting from $^{56}Fe \rightarrow {}^{58}Fe$ and $^{65}Zn \rightarrow {}^{67}Zn$ substitution for ZFO (X = 0) in its two-spin configuration, FM (top) and AFM (below); blue bars represent Fe atom, and orange bars represent the Zn atom.

https://doi.org/10.1021/acsomega.3c04268
ACS Omega 2023, 8, 36999−37010

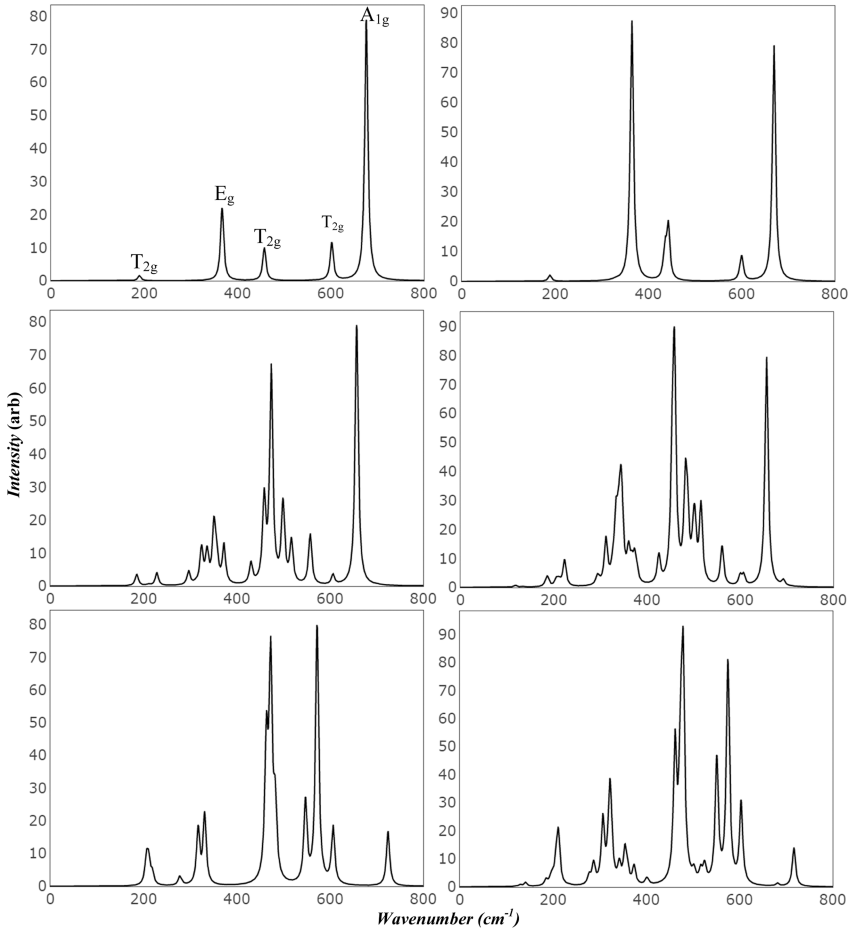

Figure 5. B3LYP simulated Raman spectra of ZFO ($X = 0.0, 0.5, 1.0$) with its two-order magnetic configuration; left panels refer to FM and right panels refer to AFM.

Table 5. Comparison of the Frequencies and Assignments of the Raman Modes of Normal ZFO Previously Reported in the Literature with Those Calculated in the Present Study

						ref 81		current study ($X = 0$)	
Raman symmetry assignment	ref 13	refs 66,83	ref 5	ref 84	ref 39	exp.	theo	FM	AFM
T_{2g} (1)	221	159	212	160	190.7	176.5 ± 3	191	189.7	188.6
E_g	246	254	230	250	296.7	352 ± 3	375	367.1	365.3
T_{2g} (2)	355	364	277, 33	350	461.9	447 ± 3	464	457.7	435.7
							472		442.9
T_{2g} (3)	451	459	496	450	550.6	573 ± 3	600	602.3	601.2
A_{1g}	647	665	589, 67	630	604.5/681	647 ± 3	695	676.6	669.7

($T_{2g}(3)$), and 458 cm^{-1} ($T_{2g}(2)$), with relative intensities of 43% and 38% compared to the highest peak. The fourth peak at 367 cm^{-1} (E_g) has a moderate intensity of about 53% of the highest peak, and the final peak is weak, appearing at a lower wavenumber (189 cm^{-1}) ($T_{2g}(1)$). However, a review of the literature reveals that the peak at 602 cm^{-1} not reported experimentally in ref 13, and assigned to A_{1g} symmetry in ref 39, leads to misleading assignments for the obtained Raman modes, as shown in Table 4. Among the various studies reviewed in ref 66, our assignment aligns only with the reported in ref 81. The observed peak at ~250 cm^{-1} [82] does not correspond to one of the five modes predicted by group theory, as indicated in ref 81. Instead, it is more likely related to cation disorder within the synthesized samples or defects. As we will see below, inversion induces a growing peak in this region. The peak at 602.3 cm^{-1} may not have been observed experimentally due to the broadening of the A_{1g} peak caused by strain development in small crystalline particles.

Analysis of the calculated spectra reveals that the highest peak A_{1g} is a combination of two modes, including the stretching of Zn−O and the bending of Zn−O−Fe, which mostly belong to AO_4. The other peaks at 602 and 189.7 cm^{-1} are a combination of many correlated bending modes involving cations in both sites. This explains the low intensities of these peaks and why they are not observed in most of the measured spectra. The peak at 457.7 cm^{-1} involves only the stretching modes of Zn−O−Fe and O−Zn−O, while the dominant mode at 367.1 cm^{-1} is the stretching of Fe−O bonds. The effect of spin reconstruction in the Raman spectra of AFM ($X = 0$) (Table 5) is primarily concentrated on three significant differences; the peak at 457.7 cm^{-1} shifts to a lower frequency and splits into two peaks, 436 and 443 cm^{-1}; the peak at 367 cm^{-1} becomes broader and more

https://doi.org/10.1021/acsomega.3c04268
ACS Omega 2023, 8, 36999−37010

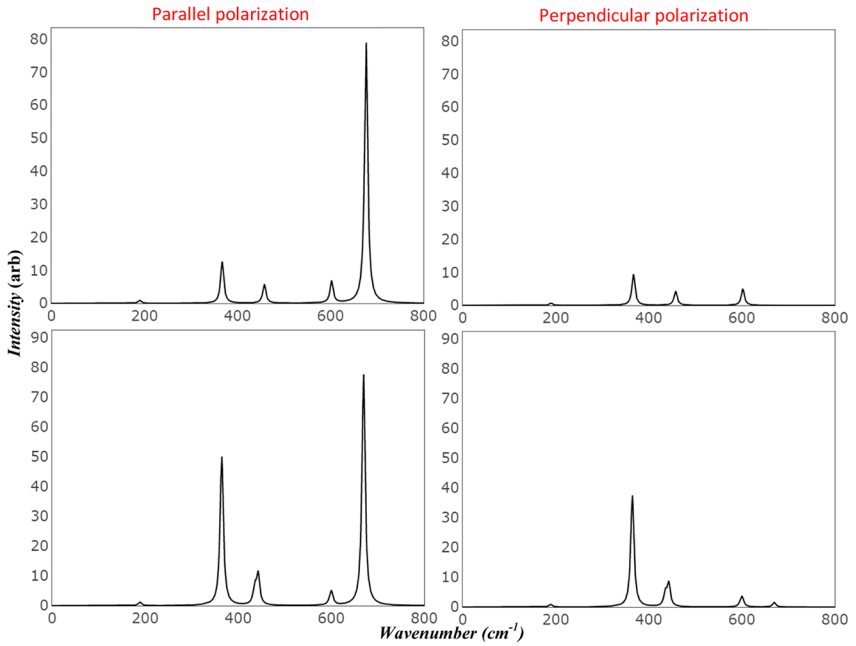

Figure 6. Polarized Raman spectra of ZFO ($X = 0$) for two-spin configurations, demonstrating the dependence of A_{1g} mode intensities on exited light direction. The top panel corresponds to FM, and the bottom panel corresponds to AFM.

intense, about 64.4% of the highest peak, and shifts slightly to a lower frequency by 3 cm^{-1}; the highest-frequency peak A_{1g} exhibits a significant red shift of approximately 7 cm^{-1}. Such influence of some Raman modes by spin reconstruction has been previously reported for magnetic material by Webster et al.,[85] and attributed to spin−orbit coupling. The splitting of the doubly degenerate peak is likely related to the slight deformation of the cubic crystal. Figure 6 presents the Raman spectra for the normal ZFO, as well as the FM and AFM phases, obtained under different polarization conditions. It is evident that the A_{1g} mode is significantly influenced by the laser setup as the corresponding peak vanishes in the spectra acquired with perpendicular polarization. This effect is also observed in the AFM spectra. The polarization dependence of these modes could provide valuable guidance for optimizing experimental setups and obtaining accurate spectral data.

The changes in the infrared (IR) spectra of the inverse ferromagnetic (FM) ZFO spinel are significant, demonstrating splitting across all spectrum regions and presenting a distinct structure compared to normal spectra. The inversion activates additional modes at low-frequency regions with very low intensities (141, 186, 194, and 205 cm^{-1}), followed by a group of peaks with high intensities (287, 313, 317, 348, and 350 cm^{-1}). Two peaks with moderate intensity appear at 376 and 408 cm^{-1}, and at a higher-wavenumber region, four peaks appear at 484, 496, 503, and 516 cm^{-1}. Captivating feature of the vibrational spectra is the distinct peak at 679 cm^{-1}, which emerges in an otherwise flat region of the normal spectrum. This peak was previously reported in ref 86 for Ni-based compositions, where it manifested as a sideband of the primary v_1 peak and was accompanied by another shoulder appearing at lower frequencies. For instance, in $(Ni_{0.99}\ Fe_{0.02})Fe_2O_4$, the bands were observed at 667.5, 605 (v_1), and 537.5 cm^{-1}, with their intensities diminishing as Zn content increased. These spectral features were attributed to the presence of Fe^{2+} cations in tetrahedral sites, causing lattice deformation. A red shift for the v_1 band was also noticed in association with the increasing intensities of the shoulders, in accordance with our calculations: 524.5 cm^{-1} in the normal spinel shifted to a range of 484−516 cm^{-1} after splitting. Interestingly, no splitting was reported for the second main band, v_2, which may be due to the low resolution of the IR instrument at low frequencies.

The intensity of the highest peak at 317 cm^{-1} is three times lower compared to the corresponding peak at 312 cm^{-1} in the normal spectrum. This occurs due to the full occupation of heavier atoms (Zn) in the B-site and lighter atoms (Fe) in the A-site. This splitting of the two main IR absorption bands into four sub-bands has been reported by Rathod et al.[87] for Li ferrite and Li−Zn ferrite compositions. Zaki et al.[3] also reported IR splitting for $Cu_{1-x}Zn_xFe_2O_4$ samples as Zn content increased, with higher wavenumbers (700, 600, 536 cm^{-1}) and lower wavenumbers (395, 325, 266 cm^{-1}) appearing for $X = 1$. The emergence of the 700 cm^{-1} peak may be linked to the formation of an inverse spinel in their study, while the low-frequency 266 cm^{-1} peak was only activated in our investigation upon inversion.

Figure 3 compares the AFM spectra with the FM of inverse ZFO spinels. The antiferromagnetic configuration results in a diminished intensity of the highest peak at 319 cm^{-1} and a subtle shift to a higher wavenumber by 3 cm^{-1}. The peak at 354 cm^{-1} experiences a 4 cm^{-1} shift while retaining the same intensity, and the peak at 287 cm^{-1} remains unchanged. Meanwhile, groups of peaks at higher frequencies shift even higher, specifically at 489, 517, and 525 cm^{-1}.

Table 6 provides a clear depiction of the distinct motion types associated with the activated modes upon inversion, particularly when X equals 0.5 and 1. The vibrational modes of the two cations become increasingly correlated as they split, with nearly all cations participating in the activated modes. A limited number of peaks display a mode that depends solely on one cation. For example, when X equals 0.5, the modes at the lower frequencies of 184 and 186 cm^{-1} and 210 cm^{-1} involve only the Zn and Fe atoms, respectively, albeit with minimal intensities. The mode with the highest intensity, at 324 cm^{-1}, along with two modes at 459 and 474 cm^{-1}, which have very low intensities,

https://doi.org/10.1021/acsomega.3c04268
ACS Omega 2023, 8, 36999−37010

Table 6. Activated Frequencies and Related Mode Types (Stretching (S) and Bending (B)) for Inverted ZFO (FM, $X = 0.5$ and 1)

wavenumber (cm^{-1}) FM $X = 0.5$	Fe−O−Fe (B)	Fe−O−Zn (B)	Zn−O−Zn (B)	O−Fe−O (B)	O−Zn−O (B)	Zn−O−Fe (S)	Fe−O−Fe (S)	Zn−O−Zn (S)	O−Fe−O (S)	O−Zn−O (S)
124		√	√							
184			√							
186					√					
210	√									
211	√	√		√						
229	√					√	√			
297		√	√					√		
312			√							
324							√			
336						√				
351	√						√			
430	√	√								
459							√			
474							√			
498		√						√		
500	√			√			√		√	
517			√					√	√	
558		√	√	√				√		
606			√	√			√	√		
657		√	√					√		√
702	√	√					√		√	
wavenumber (cm^{-1}) FM $X = 1$	Fe−O−Fe (B)	Fe−O−Zn (B)	Zn−O−Zn (B)	O−Fe−O (B)	O−Zn−O (B)	Zn−O−Fe (S)	Fe−O−Fe (S)	Zn−O−Zn (S)	O−Fe−O (S)	O−Zn−O (S)
141	√	√								
186		√								
194	√									
205		√				√				
287			√		√					
313										√
317		√		√		√				
348		√					√			
350									√	
408	√									
484							√		√	
496	√					√	√	√	√	√
503	√	√		√						
516							√		√	
679	√	√					√		√	

are correlated to the Fe atom. Furthermore, the shoulder at 312 cm^{-1} is associated with Zn. As we transition to X equaling 1, the correlation among the cation modes amplifies, with only four modes engaging a single cation. Specifically, three modes at 194, 350 (with high intensity), and 408 cm^{-1} involve Fe, while the mode at 313 cm^{-1} is associated with Zn.

The Raman spectra, akin to their IR counterparts, exhibit splitting throughout the spectrum with altered relative intensities compared to the normal spectra (Figure 5). At lower wavenumbers, the peaks at 206, 210, and 218 cm^{-1} intensify by approximately 10-fold, flattening the spectrum below 206 cm^{-1}. The trio of peaks appearing at 277, 317, and 331 cm^{-1} exhibit lower intensities compared to the corresponding E_g peak in the normal spectra. Conversely, groups at 463, 472, and 482 cm^{-1} and 547, 572, and 606 cm^{-1} reveal significantly higher intensities than the corresponding unsplit T_{2g} peaks in the normal spectra. The final nondegenerate peak at 725 cm^{-1} decreases in intensity and shifts to a higher wavenumber by 49 cm^{-1}, a consequence of the complete occupation of the lighter Fe atom at the A-site.

The AFM spectrum displays minuscule peaks at 130 and 141 cm^{-1}, with the intensity of the peak at 211 cm^{-1} nearly doubling. Splitting is observed in the group of peaks centered at the highest one, 322 cm^{-1} (278, 287, 307, 322, 343, 354, 374, 401 cm^{-1}). The peak at 462 cm^{-1} shifts to a lower wavenumber by 2 cm^{-1}, while the peaks at 479 and 502 cm^{-1} shift to higher wavenumbers by 7 and 20 cm^{-1}, respectively. Two small new peaks emerge at 517 and 525 cm^{-1}. The final group at 551 and 575 cm^{-1} shifts to higher wavenumbers by 4 and 3 cm^{-1}, respectively, and the peak at 604 cm^{-1} shifts to a lower wavenumber by 2 cm^{-1}. The ultimate peak at 717 cm^{-1} experiences a slight decrease in intensity and shifts to a lower wavenumber by 8 cm^{-1}.

4. CONCLUSIONS

In conclusion, our calculations of optimized structures, bond lengths, bond populations, and spin densities for ZFO compounds with varying inversion degrees ($X = 0$, 0.5, and 1) and spin configurations (FM and AFM) underscore the significance of Fe and Zn distribution within the A- and B-

https://doi.org/10.1021/acsomega.3c04268
ACS Omega 2023, 8, 36999−37010

sites. The Zn−O bonds exhibit a stronger preference for the tetrahedral A-site due to their larger ionic size and more significant overlap, which leads to more covalent character. The vibrational spectra of the ZFO spinel structures exhibit notable changes upon inversion and alterations in magnetic order, including peak shifts, intensity variations, and peak splitting. These spectral transformations can be attributed to the rearrangement of cations within the lattice and the impact of magnetic interactions on the vibrational modes. Our calculations successfully align with group theory's predictions for vibrational modes in the spinel structure, at 524.59, 358.48, 312.49, and 192.9 cm^{-1} for the $4T_{1u}$ IR modes, and at 676.6, 367.1, and (189.7, 457.7, 602.3) cm^{-1} for the A_{1g}, E_g, and ($3T_{2g}$) Raman modes, respectively. The IR spectra of the inverted structure exhibit a peak at 679 cm^{-1}, which emerges in a region of the spectrum that is otherwise flat in normal spectra. This peak could be linked to an inverted structure in the measured spectra. Our analysis further reveals that the rising mode at ∼250 cm^{-1} in the Raman spectra does not correspond to any of the five modes predicted by group theory, as indicated by experimental studies. This peak is activated only upon inversion. A careful analysis of the isotopic IR spectra reveals fascinating interactions and correlations between the modes, providing insights into the complexities of stretching and bending modes involving Zn and Fe atoms. Understanding these spectral alterations provides crucial insights into the local atomic environment and magnetic properties of these materials. This knowledge is invaluable when exploring their physical properties and potential applications in various sectors, such as energy storage, catalysis, and spintronics. The methodology elucidated here can be adapted and applied to explore other members of the spinel ferrite family, thereby facilitating a comprehensive interpretation of the experimental spectra.

AUTHOR INFORMATION

Corresponding Author

Tahani Saad Almutairi − *Section of Physical Chemistry Department of Chemistry, Taibah University, Madinah 42353, Saudi Arabia;* orcid.org/0000-0003-4983-7576; Email: talmutairi@taibahu.edu.sa

Complete contact information is available at: https://pubs.acs.org/10.1021/acsomega.3c04268

Notes

The author declares no competing financial interest.

ACKNOWLEDGMENTS

The author expresses profound gratitude to Taibah University, specifically the Deanship of Scientific Research, for generously providing the necessary facilities and conducive environment that enabled the successful execution of this research within the Department of Chemistry.

REFERENCES

(1) White, W.; DeAngelis, B. Interpretation of the Vibrational Spectra of Spinels. *Spectrochim. Acta, Part A* **1967**, *23* (4), 985−995.

(2) Gawas, U. B.; Verenkar, V. M. S.; Vader, V. T.; Jain, A.; Meena, S. S. Effects of Sintering Temperature on Microstructure, Initial Permeability and Electric Behaviour of Ni-Mn-Zn Ferrites. *Mater. Chem. Phys.* **2022**, *275*, No. 125250.

(3) Zaki, H. M.; Dawoud, H. A. Far-Infrared Spectra for Copper Zinc Mixed Ferrites. *Phys. B* **2010**, *405* (21), 4476−4479.

(4) Shimada, T.; Tachibana, T.; Nakagawa, T.; Yamamoto, T. Site Occupation Study of ZnFe2O4 and $NiFe_2O_4$ by Far-Infrared Reflectivity. *J. Alloys Compd.* **2004**, *379* (1−2), 122−126.

(5) Singh, J. P.; Dixit, G.; Srivastava, R. C.; Agrawal, H. M.; Kumar, R. Raman and Fourier-Transform Infrared Spectroscopic Study of Nanosized Zinc Ferrite Irradiated with 200 MeV Ag15+ Beam. *J. Alloys Compd.* **2013**, *551*, 370−375.

(6) Nekvapil, F.; Bunge, A.; Radu, T.; Cinta Pinzaru, S.; Turcu, R. Raman Spectra Tell Us so Much More: Raman Features and Saturation Magnetization for Efficient Analysis of Manganese Zinc Ferrite Nanoparticles. *J. Raman Spectrosc.* **2020**, *51* (6), 959−968.

(7) Chandramohan, P.; Srinivasan, M. P.; Velmurugan, S.; Narasimhan, S. V. Cation Distribution and Particle Size Effect on Raman Spectrum of $CoFe_2O_4$. *J. Solid State Chem.* **2011**, *184* (1), 89−96.

(8) Palacio Gómez, C. A.; Barrero Meneses, C. A.; Jaén, J. A. Raman, Infrared and Mössbauer Spectroscopic Studies of Solid-State Synthesized Ni-Zn Ferrites. *J. Magn. Magn. Mater.* **2020**, *505*, No. 166710, DOI: 10.1016/j.jmmm.2020.166710.

(9) Mazen, S. A. Infrared Absorption and Dielectric Properties of Li ± Cu Ferrite. *Mater. Chem. Phys.* **2000**, *62* (2), 139−147.

(10) Ravinder, D. Far-Infrared Spectral Studies of Mixed Lithium-Zinc Ferrites. *Mater. Lett.* **1999**, *40* (5), 205−208.

(11) Murugesan, C.; Chandrasekaran, G. Impact of Gd3+ Substitution on the Structural, Magnetic and Electrical Properties of Cobalt Ferrite Nanoparticles. *RSC Adv.* **2015**, *5* (90), 73714−73725.

(12) Hafner, S. The Absorption of Some Metal Oxides with Spinel Structure. *Z. Kristallogr.* **1961**, *115*, 331−358.

(13) Wang, Z.; Schiferl, D.; Zhao, Y.; O'Neill, H. S. C. High Pressure Raman Spectroscopy of Spinel-Type Ferrite ZnFe 2O4. *J. Phys. Chem. Solids* **2003**, *64* (12), 2517−2523.

(14) Smit, J.; Wijn, H. P. J. *Ferrites*; Cleaver-Hume Press: London, 1959.

(15) Zhao, Q.; Yan, Z.; Chen, C.; Chen, J. Spinels: Controlled Preparation, Oxygen Reduction/Evolution Reaction Application, and Beyond. *Chem. Rev.* **2017**, *117* (15), 10121−10211.

(16) Chandrasekaran, S.; Bowen, C.; Zhang, P.; Li, Z.; Yuan, Q.; Ren, X.; Deng, L. Spinel Photocatalysts for Environmental Remediation, Hydrogen Generation, CO2 Reduction and Photoelectrochemical Water Splitting. *J. Mater. Chem. A* **2018**, *6* (24), 11078−11104.

(17) Schiessl, W.; Potzel, W.; Karzel, H.; Steiner, M.; Kalvius, G.; Martin, A.; Krause, M.; Halevy, I.; Gal, J.; Schafer, W.; will, G.; et al. Magnetic Properties of the $ZnFe_2O_4$ Spinel. *Phys. Rev. B* **1996**, *53* (14), 9143.

(18) Najafi Birgani, A.; Niyaifar, M.; Hasanpour, A. Study of Cation Distribution of Spinel Zinc Nano-Ferrite by X-Ray. *J. Magn. Magn. Mater.* **2015**, *374*, 179−181.

(19) O'Neill; Hugh St, C.; Navrotsky, A. Simple Spinels: Crystallographic Parameters, Cation Radii, Lattice Energies, and Cation Distribution. *Am. Mineral.* **1983**, *68* (1), 181−194.

(20) Priamushko, T.; Guggenberger, P.; Mautner, A.; Lee, J.; Ryoo, R.; Kleitz, F. Enhancing OER Activity of Ni/Co Oxides via Fe/Mn Substitution within Tailored Mesoporous Frameworks. *ACS Appl. Energy Mater.* **2022**, *5* (11), 13385−13397.

(21) Jauhar, S.; Kaur, J.; Goyal, A.; Singhal, S. Tuning the Properties of Cobalt Ferrite: A Road towards Diverse Applications. *RSC Adv.* **2016**, *6* (100), 97694−97719.

(22) Pham, T. N.; Huy, T. Q.; Le, A.-T. Spinel Ferrite (AFe2O4)-Based Heterostructured Designs for Lithium-Ion Battery, Environmental Monitoring, and Biomedical Applications. *RSC Adv.* **2020**, *10* (52), 31622−31661.

(23) Fan, G.; Tong, J.; Li, F. Visible-Light-Induced Photocatalyst Based on Cobalt-Doped Zinc Ferrite Nanocrystals. *Ind. Eng. Chem. Res.* **2012**, *51* (42), 13639−13647.

(24) Sharma, S.; Dutta, V.; Raizada, P.; Hosseini-Bandegharaei, A.; Thakur, V.; Nguyen, V.-H.; VanLe, Q.; Singh, P. An Overview of Heterojunctioned ZnFe2O4 Photocatalyst for Enhanced Oxidative Water Purification. *J. Environ. Chem. Eng.* **2021**, *9* (5), No. 105812.

(25) Wu, K.; Li, J.; Zhang, C. Zinc Ferrite Based Gas Sensors: A Review. *Ceram. Int.* **2019**, *45* (9), 11143−11157.
(26) NuLi, Y.-N.; Chu, Y.-Q.; Qin, Q.-Z. Nanocrystalline ZnFe2 O 4 and Ag-Doped ZnFe2 O 4 Films Used as New Anode Materials for Li-Ion Batteries. *J. Electrochem. Soc.* **2004**, *151* (7), A1077.
(27) Vedernikova, I. A. Magnetic Nanoparticles: Advantages of Using, Methods for Preparation, Characterization, Application in Pharmacy. *Rev. J. Chem.* **2015**, *5* (3), 256−280.
(28) Kefeni, K. K.; Msagati, T. A.; Nkambule, T. T.; Mamba, B. B. Spinel Ferrite Nanoparticles and Nanocomposites for Biomedical Applications and Their Toxicity. *Mater. Sci. Eng., C* **2020**, *107*, No. 110314.
(29) Emori, S.; Li, P. Ferrimagnetic Insulators for Spintronics: Beyond Garnets. *J. Appl. Phys.* **2021**, *129* (2), No. 020901, DOI: 10.1063/5.0033259.
(30) Jin, C.; Li, P.; Mi, W.; Bai, H. Structure, Magnetic, and Transport Properties of Epitaxial ZnFe2O4 Films: An Experimental and First-Principles Study. *J. Appl. Phys.* **2014**, *115* (21), No. 213908.
(31) Waldron, R. D. Infrared Spectra of Ferrites. *Phys. Rev.* **1955**, *99* (6), 1727.
(32) Andrés-Vergés, M.; De Julian, C.; Gonz'alez, J.; Serna, C. Preparation and Magnetic Properties of Monodispersed Zn Ferrites of Submicrometric Size. *J. Mater. Sci.* **1993**, *28*, 2962−2966.
(33) Lazarević, Z.; Milutinović, A. N.; Jovalekić, Č. D.; Ivanovski, V. N.; Daneu, N.; Macrossed, D.; Signarević, I.; Romčević, N. Spectroscopy Investigation of Nanostructured Nickel-Zinc Ferrite Obtained by Mechanochemical Synthesis. *Mater. Res. Bull.* **2015**, *63*, 239−247.
(34) Yadav, R. S.; Kuřitka, I.; Vilcakova, J.; Urbánek, P.; Machovsky, M.; Masař, M.; Holek, M. Structural, Magnetic, Optical, Dielectric, Electrical and Modulus Spectroscopic Characteristics of ZnFe2O4 Spinel Ferrite Nanoparticles Synthesized via Honey-Mediated Sol-Gel Combustion Method. *J. Phys. Chem. Solids* **2017**, *110*, 87−99.
(35) Zhang, Y.; Shi, Q.; Schliesser, J.; Woodfield, B. F.; Nan, Z. Magnetic and Thermodynamic Properties of Nanosized Zn Ferrite with Normal Spinal Structure Synthesized Using a Facile Method. *Inorg. Chem.* **2014**, *53* (19), 10463−10470.
(36) Moustafa, A. M.; Salah, L. M.; Salerno, M.; Abdellatif, M. H. Symmetry in Magnetic and Vibrational Spectra of Multi-Element Spinel Ferrite. *J. Magn. Magn. Mater.* **2020**, *513*, No. 167267, DOI: 10.1016/j.jmmm.2020.167267.
(37) Angadi, V. J.; Anupama, A. V.; Kumar, R.; Choudhary, H. K.; Matteppanavar, S.; Somashekarappa, H. M.; Rudraswamy, B.; Sahoo, B. Composition Dependent Structural and Morphological Modifications in Nanocrystalline Mn-Zn Ferrites Induced by High Energy γ-Irradiation. *Mater. Chem. Phys.* **2017**, *199*, 313−321.
(38) López, F.; Lopez-Delgado, A.; Martın de Vidales, J.; Vila, E. Synthesis of Nanocrystalline Zinc Ferrite Powders from Sulphuric Pickling Waste Water. *J. Alloys Compd.* **1998**, *265*, 291−296.
(39) Andhare, D. D.; Patade, S. R.; Jadhav, S. A.; Somvanshi, S. B.; Jadhav, K. M. Rietveld Refined Structural, Morphological, Raman and Magnetic Investigations of Superparamagnetic Zn−Co Nanospinel Ferrites Prepared by Cost-Effective Co-Precipitation Route. *Appl. Phys. A: Mater. Sci. Process.* **2021**, *127* (6), No. 480, DOI: 10.1007/s00339-021-04603-9.
(40) Almessiere, M. A.; Unal, B.; Korkmaz, A. D.; Shirsath, S. E.; Baykal, A.; Slimani, Y.; Gondal, M.; Baig, U.; Trukhanov, A. Electrical and Dielectric Properties of Rare Earth Substituted Hard-Soft Ferrite $(Co_{0.5}Ni_{0.5}Ga_{0.01}Gd_{0.01}Fe_{1.98}O_4)$ x/$(ZnFe_2O_4)$ y Nanocomposites. *J. Mater. Res. Technol.* **2021**, *15*, 969−983.
(41) Jotania, R. B.; Nandotaria, R. A.; Chauhan, C. C.; Hashim, M.; Meena, S. S.; Shirsath, S. E. Structural Phases and Maxwell–Wagner Relaxation in Magnetically Soft-$ZnFe_2O_4$ and Hard-$Sr_2Cu_2Fe_{12}O_{22}$ Nanocomposites. *Ceram. Int.* **2016**, *42* (2), 2289−2298.
(42) Ghasemi, A.; Sepelak, V.; Shirsath, S. E.; Liu, X.; Morisako, A. Mossbauer Spectroscopy and Magnetic Characteristics of $Zn_{1-X}Co_xFe_2O_4$ (X= 0−1) Nanoparticles. *J. Appl. Phys.* **2011**, *109* (7), No. 07A512, DOI: 10.1063/1.3553777.
(43) Singh, D. J.; Gupta, M.; Gupta, R. Density-Functional Description of Spinel $ZnFe_2O_4$. *Phys. Rev. B* **2001**, *63* (20), No. 205102.
(44) Cheng, C. Long-Range Antiferromagnetic Interactions in $ZnFe_2O_4$ and $CdFe_2O_4$: Density Functional Theory Calculations. *Phys. Rev. B* **2008**, *78* (13), No. 132403.
(45) Soliman, S.; Elfalaky, A.; Fecher, G. H.; Felser, C. Electronic Structure Calculations for ZnFe2O4. *Phys. Rev. B* **2011**, *83* (8), No. 085205.
(46) Rodríguez Torres, C. E.; Pasquevich, G. A.; Zélis, P. M.; Golmar, F.; Heluani, S. P.; Nayak, S. K.; Adeagbo, W. A.; Hergert, W.; Hoffmann, M.; Ernst, A.; Esquinazi, P.; Stewart, S. J. Oxygen-Vacancy-Induced Local Ferromagnetism as a Driving Mechanism in Enhancing the Magnetic Response of Ferrites. *Phys. Rev. B* **2014**, *89* (10), No. 104411.
(47) Jin, C.; Li, P.; Mi, W.; Bai, H. Structure, Magnetic, and Transport Properties of Epitaxial ZnFe2O4 Films: An Experimental and First-Principles Study. *J. Appl. Phys.* **2014**, *115* (21), No. 213908.
(48) Chamritski, I.; Burns, G. Infrared- And Raman-Active Phonons of Magnetite, Maghemite, and Hematite: A Computer Simulation and Spectroscopic Study. *J. Phys. Chem. B* **2005**, *109* (11), 4965−4968.
(49) Dovesi, R.; Orlando, R.; Erba, A.; Zicovich-wilson, C. M.; Civalleri, B.; Casassa, S.; Maschio, L.; Ferrabone, M.; Pierre, M. D. L.; Arco, P. D.; No, Y.; Caus, M. CRYSTAL14 : A Program for the Ab Initio Investigation of Crystalline Solids. In *International Journal of Quantum Chemistry*; Wiley Online Library, 2014; pp 1287−1317.
(50) Becke, A. D. Density-functional Thermochemistry. I. The Effect of the Exchange-only Gradient Correction. *J. Chem. Phys.* **1992**, *96* (96), 2155−2160.
(51) Adamo, C.; Barone, V. Toward Chemical Accuracy in the Computation of NMR Shieldings: The PBE0Model. *Chem. Phys. Lett.* **1998**, *298* (1−3), 113−119.
(52) Krukau, A. V.; Vydrov, O. A.; Izmaylov, A. F.; Scuseria, G. E. Influence of the Exchange Screening Parameter on the Performance of Screened Hybrid Functionals. *J. Chem. Phys.* **2006**, *125* (22), No. 224106.
(53) Jaffe, J. E.; H, A. Hartree-Fock Study of Phase Changes in ZnO at High Pressure. *Phys. Rev. B* **1993**, *48* (11), 7903.
(54) Catti, M.; Valerio, G.; Dovesi, R. Theoretical Study of Electronic, Magnetic, and Structural Properties of α-Fe2O3 (Hematite). *Phys. Rev. B* **1995**, *51* (12), 7441−7450.
(55) Towler, M. D.; Allan, N.; Harrison, N. M.; Saunders, V.; Mackrodt, W.; Apra, E. Ab Initio Study of MnO and NiO. *Phys. Rev. B* **1994**, *50* (8), 5041.
(56) Monkhorst, H. J.; Pack, J. D. Special Points for Brillouin-Zone Integrations. *Phys. Rev. B* **1976**, *13* (12), 5188−5192.
(57) Pisani, C.; Dovesi, R.; Roetti, C. *Hartree-Fock Ab Initio Treatment of Crystalline Systems*, Lecture Notes in Chemistry; Springer Berlin Heidelberg, 2012.
(58) Mulliken, R. S. Electronic Population Analysis on LCAO-MO Molecular Wave Functions. I. *J. Chem. Phys.* **1955**, *23* (10), 1833−1840.
(59) Zicovich-Wilson, C. M.; Pascale, F.; Roetti, C.; Saunders, V. R.; Orlando, R.; Dovesi, R. Calculation of the Vibration Frequencies of α-Quartz: The Effect of Hamiltonian and Basis Set. *J. Comput. Chem.* **2004**, *25* (15), 1873−1881.
(60) Pascale, F.; Zicovich-Wilson, C. M.; Lopez, F.; Civalleri, B.; Orlando, R.; D, R. The Calculation of the Vibrational Frequencies of Crystalline Compounds and Its Implementation in the CRYSTAL Code. *J. Comput. Chem.* **2004**, *25*, 888−897.
(61) Maschio, L.; Kirtman, B.; Rérat, M.; Orlando, R.; Dovesi, R. Ab Initio Analytical Raman Intensities for Periodic Systems through a Coupled Perturbed Hartree-Fock/Kohn-Sham Method in an Atomic Orbital Basis. I. Theory. *J. Chem. Phys.* **2013**, *139* (16), No. 164101, DOI: 10.1063/1.4824442.
(62) Maschio, L.; Kirtman, B.; Orlando, R.; Rèrat, M. Ab Initio Analytical Infrared Intensities for Periodic Systems through a Coupled Perturbed Hartree-Fock/Kohn-Sham Method. *J. Chem. Phys.* **2012**, *137* (20), No. 204113, DOI: 10.1063/1.4767438.
(63) Hess, B. A., Jr; Schaad, L. J.; Carsky, P.; Zahradnik, R. Ab Initio Calculations of Vibrational Spectra and Their Use in the Identification of Unusual Molecules. *Chem. Rev.* **1986**, *86* (4), 709−730.

https://doi.org/10.1021/acsomega.3c04268
ACS Omega 2023, 8, 36999−37010

(64) Ferrero, M.; Ŕrat, M.; Orlando, R.; Dovesi, R. Coupled Perturbed Hartree-Fock for Periodic Systems: The Role of Symmetry and Related Computational Aspects. *J. Chem. Phys.* **2008**, *128* (1), No. 014110, DOI: 10.1063/1.2817596.
(65) Fritsche, O. Electronic and Optical Properties of Spinel Zinc Ferrite: Ab Initio Hybrid Functional Calculations. *J. Phys.: Condens. Matter* **2018**, *30* (9), No. 095502.
(66) Galinetto, P.; Albini, B.; Bini, M.; Mozzati, M. C. Raman Spectroscopy in Zinc Ferrites Nanoparticles. In *Raman Spectroscopy*; InTech, 2018; Vol. *223*.
(67) Kamazawa, K.; Tsunoda, Y.; Kadowaki, H.; Kohn, K. Magnetic Neutron Scattering Measurements on a Single Crystal of Frustrated $ZnFe_2O_4$. *Phys. Rev. B* **2003**, *68* (2), No. 024412.
(68) Usa, T.; Kamazawa, K.; Sekiya, H.; Nakamura, S.; Tsunoda, Y.; Kohn, K.; Tanaka, M. Magnetic Properties of ZnFe2O4 as a 3-D Geometrical Spin Frustration System. *J. Phys. Soc. Jpn.* **2004**, *73* (10), 2834−2840.
(69) Waerenborgh, J.; Figueiredo, M.; Cabral, J.; Pereira, L. Temperature and Composition Dependence of the Cation Distribution in Synthetic $ZnFe_yAl_{2-Y}O_4$ ($0 \leq Y \leq 1$) Spinels. *J. Solid State Chem.* **1994**, *111* (2), 300−309.
(70) Kamazawa, K.; Tsunoda, Y.; Odaka, K.; Kohn, K. Magnetic Neutron Scattering Measurements on a Single Crystal of Frustrated ZnFe2O4. *J. Phys. Chem. Solids* **1999**, *60* (8−9), 1261−1264.
(71) Henderson, C. M. B.; Charnock, J. M.; Plant, D. A. Cation Occupancies in Mg, Co, Ni, Zn, Al Ferrite Spinels: A Multi-Element EXAFS Study. *J. Phys.: Condens. Matter* **2007**, *19* (7), No. 076214.
(72) Takaobushi, J.; Ishikawa, M.; Ueda, S.; Ikenaga, E.; Kim, J. J.; Kobata, M.; Takeda, Y.; Saitoh, Y.; Yabashi, M.; Nishino, Y.; Miwa, D.; Tamasaku, K.; Ishikawa, T.; Satoh, I.; Tanaka, H.; Kobayashi, K.; Kawai, T. Electronic Structures of $Fe_{3-X}M_xO_4$ (M = Mn,Zn) Spinel Oxide Thin Films Investigated by x-Ray Photoemission Spectroscopy and x-Ray Magnetic Circular Dichroism. *Phys. Rev. B* **2007**, *76* (20), No. 205108.
(73) Ziaei, V.; Bredow, T. Ab-Initio Optical Properties and Dielectric Response of Open-Shell Spinel Zinc Ferrite. *Eur. Phys. J. B* **2017**, *90*, No. 29.
(74) Mitchell, D. W.; Das, T. P.; Potzel, W.; Schiessl, W.; Karzel, H.; Steiner, M.; Köfferlein, M.; Hiller, U.; Kalvius, G. M.; Martin, A.; Schäfer, W.; Will, G.; Halevy, I.; Gal, J. Ab Initio Electric-Field Gradients and Electron Densities at 27 Al, 57 Fe, and 67 Zn in the Spinels $ZnAl_2O_4$ and $ZnFe_2O_4$. *Phys. Rev. B* **1996**, *53* (12), 7684.
(75) Böntgen, T.; Brachwitz, K.; Schmidt-Grund, R.; Lorenz, M.; Grundmann, M. Vacuum Ultraviolet Dielectric Function of $ZnFe_2O_4$ Thin Films. *J. Appl. Phys.* **2013**, *113* (7), No. 073503.
(76) Preudhomme, J.; Tarte, P. Infrared Studies of Spinels—II: The Experimental Bases for Solving the Assignment Problem. *Spectrochim. Acta, Part A* **1971**, *27* (6), 845−851.
(77) Preudhomme, J.; Tarte, P. Infrared Studies of Spinels—III: The Normal II–III Spinels. *Spectrochim. Acta, Part A* **1971**, *27* (9), 1817−1835.
(78) Tarte, P. Etude Infra-Rouge Des Orthosilicates et Des Orthogermanates—III: Structures Du Type Spinelle. *Spectrochim. Acta* **1963**, *19* (1), 25−47.
(79) El-Sayed, A. M. Influence of Zinc Content on Some Properties of Ni-Zn Ferrites. *Ceram. Int.* **2002**, *28* (4), 363−367.
(80) Ladgaonkar, B. P.; Kolekar, C.; Vaingankar, A. Infrared Absorption Spectroscopic Study of Nd3+ Substituted Zn-Mg Ferrites. *Bull. Mater. Sci.* **2002**, *25*, 351−354.
(81) Granone, L. I.; Ulpe, A. C.; Robben, L.; Klimke, S.; Jahns, M.; Renz, F.; Gesing, T. M.; Bredow, T.; Dillert, R.; Bahnemann, D. W. Effect of the Degree of Inversion on Optical Properties of Spinel ZnFe2O4. *Phys. Chem. Chem. Phys.* **2018**, *20* (44), 28267−28278.
(82) Chand, P.; V, S.; K, P. Structural, Optical and Dielectric Properties of Transition Metal (MFe2O4; M= Co, Ni and Zn) Nano Ferrites. *Phys. B* **2017**, *524*, 53−63.
(83) Virumbrales-Del Olmo, M.; Delgado-Cabello, A.; Andrada-Chacón, A.; Sánchez-Benítez, J.; Urones-Garrote, E.; Blanco-Gutiérrez, V.; Torralvo, M. J.; Sáez-Puche, R. Effect of Composition and Coating on the Interparticle Interactions and Magnetic Hardness of MFe_2O_4 (M = Fe, Co, Zn) Nanoparticles. *Phys. Chem. Chem. Phys.* **2017**, *19* (12), 8363−8372.
(84) Lazarević, Z. Z.; Jovalekić, C.; Milutinović, A.; Sekulić, D.; Slankamenac, M.; Romčević, M.; Romčević, N. Z. Study of $NiFe_2O_4$ and $ZnFe_2O_4$ Spinel Ferrites Prepared by Soft Mechanochemical Synthesis. *Ferroelectrics* **2013**, *448* (1), 1−11.
(85) Webster, L.; Liang, L.; Yan, J.-A. Distinct Spin-Lattice and Spin-Phonon Interactions in Monolayer Magnetic CrI3. *Phys. Chem. Chem. Phys.* **2018**, *20* (36), 23546−23555.
(86) Potakova, V.; Zverev, N.; Romanov, V. On the Cation Distribution in $Ni_{1-x-Y}FeZn_yFeO_4$ Spinel Ferrites. *Phys. Status Solidi A* **1972**, *12* (2), 623−627.
(87) Rathod, V.; Anupama, A. V.; Kumar, R. V.; Jali, V. M.; Sahoo, B. Correlated Vibrations of the Tetrahedral and Octahedral Complexes and Splitting of the Absorption Bands in FTIR Spectra of Li-Zn Ferrites. *Vib. Spectrosc.* **2017**, *92*, 267−272.